Multi-Spectral Reflection Matrix for Ultra-Fast 3D Label-Free Microscopy

Paul Balondrade, Victor Barolle, Nicolas Guigui, Emeric Auriant, Nathan Rougier, Claude Boccara, Mathias Fink, Alexandre Aubry

Multi-Spectral Reflection Matrix for Ultra-Fast 3D Label-Free Microscopy

Paul Balondrade[†], Victor Barolle[†], Nicolas Guigui, Emeric Auriant,
Nathan Rougier, Claude Boccara, Mathias Fink, and Alexandre Aubry[*]
Institut Langevin, ESPCI Paris,
PSL University, CNRS, 75005 Paris, France
[†] These authors equally contributed to this work.
[*]Corresponding author (e-mail: alexandre.aubry@espci.fr)

(Dated: September 20, 2023)

Abstract

Label-free microscopy exploits light scattering to obtain a three-dimensional image of biological tissues. However, light propagation is affected by aberrations and multiple scattering, which drastically degrade the image quality and limit the penetration depth. Multi-conjugate adaptive optics and time-gated matrix approaches have been developed to compensate for aberrations but the associated frame rate is extremely limited for 3D imaging. Here we develop a multi-spectral matrix approach to solve these fundamental problems. Based on an interferometric measurement of a polychromatic reflection matrix, the focusing process can be optimized in post-processing at any voxel by addressing independently each frequency component of the wave-field. A proof-of-concept experiment demonstrates the three-dimensional image of an opaque human cornea over a 0.1 mm^3-field-of-view at a 290 nm-resolution and a 1 Hz-frame rate. This work paves the way towards a fully-digital microscope allowing real-time, in-vivo, quantitative and deep inspection of tissues.

Introduction

Imaging of thick scattering tissues remains the greatest challenge in label-free microscopy[1,2]. On the one hand, short-scale inhomogeneities of the refractive index backscatter light and the reflected wave-field can be leveraged to provide a structural image of the sample. On the other hand, larger-scale inhomogeneities give rise to forward multiple scattering events that distort the incident and reflected wave-fronts. This phenomenon, known as aberration, leads to a drastic degradation of resolution and contrast at depths greater than the scattering mean free path ℓ_s ($\sim$100 μm in biological tissues).

To circumvent this issue, adaptive optics (AO) has been transposed from astronomy to microscopy for the last twenty years[3]. The basic idea is to compensate for wave distortions either by a direct sampling of the wave-field generated by a guide star or by an indirect metric optimization of the image. Unfortunately, AO correction is limited to a finite area, the so-called isoplanatic patch, the area over which aberrations can be considered spatially invariant. This problem becomes particularly important for deep imaging, where each isoplanatic patch reduces to a speckle grain at depths larger than the transport mean free path ℓ_t ($\sim$ 1 mm in biological tissues). Multi-conjugate AO could increase the corrected field-of-view[4], but this would be at the price of a much more complex optical setup and an extremely long optimization process[5].

More recently, following seminal works that proposed post-processing computational strategies for AO[6–9], a reflection matrix approach has been developed for deep imaging[10–16]. The basic idea is to illuminate the sample by a set of input wave-fronts and record via interferometry the reflected wave-front on a camera. Once this reflection matrix is measured, a set of matrix operations can be applied in order to perform a local compensation of aberrations and restore a diffraction-limited resolution for each pixel of the field-of-view. Nevertheless, the existing approaches suffer from several limitations. In most experimental works[10,11,13–16],

the reflection matrix is time-gated around the ballistic time as usually performed in time-domain OCT[17]. Such a measurement has one main advantage since it enables the temporal filtering of most multiply-scattered photons[18]. However, it also suffers from two strong drawbacks. First, time-gating means that a large part of the information on the medium is discarded: Only the weakly distorted paths are recorded and can be compensated by a spatial phase modulation of the incident and reflected wave-fronts. Second, volumetric imaging can only be obtained by a mechanical axial scanning of the sample, which limits the frame rate Fps to, at best, 10^6 pixels.s^{-1} for a high quality correction over millimetric FOVs.

To go beyond, an acquisition of a spectral reflection matrix is required in order to capture all the information required for the three-dimensional imaging of a sample. In recent works[19,20], the spatio-temporal degrees of freedom exhibited by the reflection matrix have been exploited for tailoring dispersive focusing laws. However, the acquisition rate was slow ($Fps \sim 10^3$ pixels.s^{-1}) because the number of input wave-fronts scaled as the number of voxels in the image. Moreover, the experimental demonstration was limited to the imaging of a resolution target through a scattering medium[19,20] or a sparse medium made of colloidal particles[20]. In this paper, we go beyond an academic proof-of-concept and address the extremely challenging case of ultra-fast 3D imaging of biological tissues themselves (nerves, cells, collagen, extracellular matrix etc.). In particular, we will show how the number of input wave-fronts can be drastically decreased by deterministic focusing operations applied to the reflection matrix guided by a self-portrait of the focusing process.

To that aim, we report on a measurement of the multi-spectral reflection matrix at a much higher frame rate ($Fps \sim 10^{10}$ pixels.s^{-1}), with a 3D imaging demonstration on an *ex-vivo* opaque cornea at a resolution of 0.29 μm and 1.1 μm in the transverse and axial directions, respectively. The experimental set up combines a Fourier-domain full-field OCT (FD-FF-OCT) setup[21–23] with a coherent

multi-illumination scheme. Capable of recording a polychromatic reflection matrix of 10^{10} coefficients in less than 1 s with an ultra-fast camera, this device is fully compatible with future *in-vivo* applications. As in FD-FF-OCT, a spectral Fourier transform and numerical refocusing can provide a 3D image of the sample for each incident wave-front[21–23] but, as expected, multiple scattering is shown to strongly hamper the imaging process. A coherent compound of images obtained for each illumination in post-processing can then provide a confocal image but its resolution and contrast are drastically affected by sample-induced aberrations. Interestingly, matrix imaging can go beyond by decoupling input and output focusing points at each time-of-flight. A focused reflection matrix is synthesized and measures the cross-talk between each point inside the sample. While previous works only considered focusing points at the same depth[11–14], we show here that their axial scan gives access to a self-portrait of the light focusing process. A minimization of the point spread function extension enables an autofocus process at each depth of the sample. Finally, a compensation of transverse aberrations is performed by means of a local analysis of wave distortions[16]. A digital clearing of long-scale refractive index heterogeneities is thus applied and a three-dimensional image of the sample is obtained with an optimized contrast and close-to-ideal resolution throughout the volume.

Results

Recording the Multi-Spectral Reflection Matrix.

3D matrix imaging is based on the measurement of a multi-spectral reflection matrix from the scattering sample. The experimental setup and procedure are described in Fig. 1 (see Methods and Supplementary Figure S1). Inspired by spectral domain FFOCT[24], it simply consists in a Linnik interferometer (Fig. 1a). In the first arm, a reference mirror is placed in the focal plane of a microscope objective (MO). The second arm contains the scattering sample to be imaged through an identical MO. This interferometer is illuminated by a swept source through two

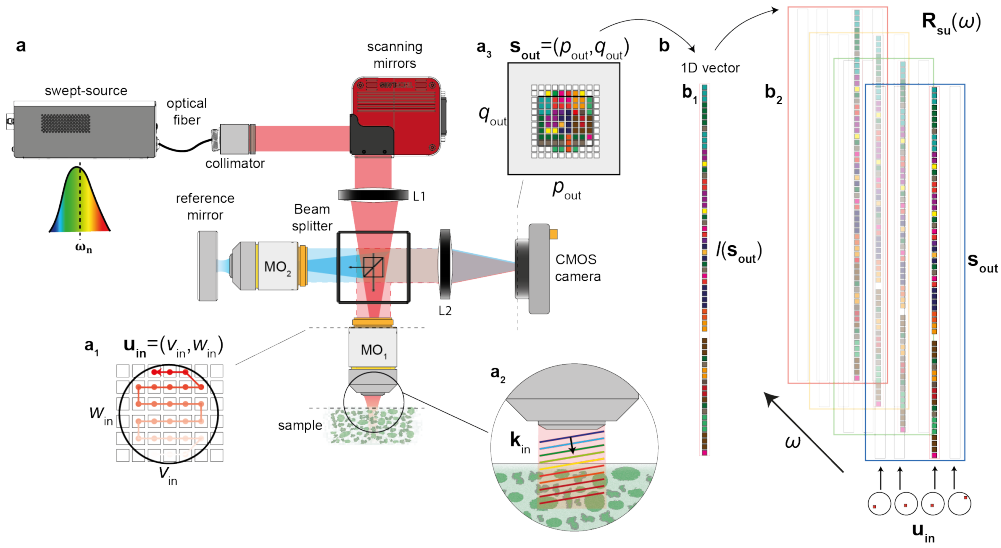

FIG. 1. **Measuring the multi-spectral reflection matrix.** **a**, A wavelength swept light source illuminates a Linnik interferometer through a collimator, two scanning mirrors and a lens (L1) that allows a raster scanning of the focal spot in the MO pupil planes ($\mathbf{u}_{\text{in}}$) in each arm ($\mathbf{a}_1$). The sample placed in the focal plane of the first MO (MO_1, NA=0.8) is thus illuminated by a set of plane waves at each frequency of the light source bandwidth ($\mathbf{a}_2$). The backscattered wave field is collected through the same MO, focused by means of a second lens L2 on the surface of a CMOS camera where it interferes with a reference beam ($\mathbf{a}_3$). The latter beam results from the reflection of the same incident wave-fronts by a reference mirror placed in the focal plane of the second MO (MO_2, NA=0.8). **b**, At each frequency ω, for each input wave-front $\mathbf{u}_{\text{in}}$, the interferogram $I(\mathbf{s}_{\text{out}})$ ($\mathbf{b}_1$) recorded by each pixel $\mathbf{s}_{\text{out}}$ of the camera provides one column of the spectral reflection matrix $\mathbf{R}_{\mathbf{su}}(\omega) = [R(\mathbf{s}_{out}, \mathbf{u}_{in}, \omega)]$ ($\mathbf{b}_2$).

scanning mirrors and a lens that allows a raster scanning of the focal spot in the MO pupil planes (Fig. 1a$_1$). The sample and reference mirror are thus illuminated by a set of plane waves at each frequency of the light source bandwidth (Fig. 1a$_2$). The reflected waves are collected through the same MOs and, ultimately, interfere on a camera conjugated with the focal plane. For each input wave-front of coordinate $\mathbf{u}_{\text{in}}$ in the pupil plane, the interferogram $I(\mathbf{s}_{\text{out}}, \mathbf{u}_{\text{in}}, \omega)$ recorded at frequency ω (Fig. 1a$_3$) provides one column of the reflection matrix $\mathbf{R}_{\mathbf{su}} = [R(\mathbf{s}_{\text{out}}, \mathbf{u}_{\text{in}}, \omega)]$ (see Methods and Fig. 1b), where $\mathbf{s}_{\text{out}}$ is the transverse location of each camera

sensor.

In the opaque cornea experiment, the reflection matrix $\mathbf{R}$ is measured with $N_{in} = 177$ plane waves, corresponding to a full scan of the immersion MO pupil (NA=0.8, refractive index $n_0 = 1.33$). The interferograms are recorded by $N_{out} = 1024^2$ pixels of the camera, corresponding to an output FOV of $\Omega_{out} \times \Omega_{out} = 297 \times 297\ \mu\text{m}^2$, with a spatial sampling $\delta\rho_{\text{out}} = 290$ nm. Finally, $N_\omega = 201$ independent frequencies are used to probe the sample within the frequency bandwidth [800; 875] nm of the light source. All the information about the sample is thus contained in the 10^{10} coefficients acquired in 1.4 s. In the following, we show how to post-process this wealth of optical data to build a 3D highly-contrasted image of the cornea at a diffraction-limited resolution.

Ultra-fast Three-Dimensional Imaging.

To that aim, the most direct path is to perform, a Fourier transform over frequency ω of the back-scattered wave-field recorded for one illumination[21]: This is the principle of FF-SS-OCT which provides an image whose axial dimension is dictated by photons' times-of-flight (Supplementary Section S2). In the present case, the resulting image is, however, completely blurred without any connection with the sample reflectivity (Supplementary Figure S2). Indeed, a high NA implies a very restricted depth-of-field ($\delta z_f \sim 2n_0\lambda/NA^2 \sim 3.5\ \mu$m), which is prohibitory for 3D imaging. A prior numerical focusing of the wave-field recorded by the camera shall be performed at each depth z of the sample. This is the principle of the holoscope developed by Hillmann *et al.* about a decade ago[9].

This numerical focusing process is performed by means of Fresnel propagators. For this purpose, the multi-spectral reflection matrix should be first projected in the output pupil plane ($\mathbf{u}_{\text{out}}$) by a simple 2D spatial Fourier transform:

$$\mathbf{R}_{\mathbf{uu}}(\omega) = \mathbf{T}^*_{\mathbf{us}}(\omega) \times \mathbf{R}_{\mathbf{su}}(\omega) \tag{1}$$

where $\mathbf{T_{us}} = [T(\mathbf{u}, \mathbf{s})]$ is the Fourier transform operator:

$$T(\mathbf{u}, \mathbf{s}, \omega) = e^{-j\frac{\omega}{c_0}\frac{\mathbf{u}\cdot\mathbf{s}}{f}} \tag{2}$$

with f, the focal length of the MOs and c_0 the vacuum light velocity. A Fresnel propagator is then applied at the output of $\mathbf{R_{uu}}(\omega)$ to numerically shift the focal plane, originally located in the middle of the sample ($z = 0$) to any depth z:

$$\mathbf{R}_{\boldsymbol{\rho}\mathbf{u}}(z, \omega) = [\mathbf{T}^{\top}_{\mathbf{u}\boldsymbol{\rho}}(\omega) \circ \mathbf{F_u}(z, \omega)] \times \mathbf{R_{uu}}(\omega) \tag{3}$$

where the symbol $\circ$ accounts for the Hadamard (term-by-term) product. $\mathbf{F_u}(z, \omega)$ is a phase mask that accounts for the propagation of each plane wave of transverse wave vector $\mathbf{k}_{||} = \omega\mathbf{u}/(c_0 f)$ over a thickness z of the sample:

$$F(\mathbf{u}, z, \omega) = e^{-j\left(\frac{n_0\omega}{c_0} - k_z\right)z}\mathcal{O}(\mathbf{u}) \tag{4}$$

with

$$k_z = \frac{\omega}{c_0}\sqrt{n_0^2 - \frac{||\mathbf{u}||^2}{f^2}}, \tag{5}$$

the longitudinal component of the wave vector, and $\mathcal{O}(\mathbf{u})$, the finite pupil support: $\mathcal{O}(\mathbf{u}) = 1$ for $||\mathbf{u}|| < fNA$ and zero elsewhere. Each reflection matrix $\mathbf{R}_{\boldsymbol{\rho}\mathbf{u}}(z, \omega) = [R(\boldsymbol{\rho}_{\text{out}}, \mathbf{u}_{\text{in}}, z, \omega)]$ connects each output virtual focusing point $\mathbf{r}_{\text{out}} = (\boldsymbol{\rho}_{\text{out}}, z)$ to each input illumination $\mathbf{u}_{\text{in}}$ at frequency ω.

Each frequency component of $\mathbf{R}_{\boldsymbol{\rho}\mathbf{u}}(z, \omega)$ should then be recombined in order to time gate the singly-scattered photons. In practice, an inverse Fourier transform over frequency ω is performed and yields an $\mathbf{R}-$matrix as a function of photon's time-of-flight t:

$$\mathbf{R}_{\boldsymbol{\rho}\mathbf{u}}(z, t) = \int d\omega \mathbf{R}_{\boldsymbol{\rho}\mathbf{u}}(z, \omega)e^{j\omega t}. \tag{6}$$

At each time t, the single scattering contribution of the wave-field corresponds to

photons that have been scattered in a coherence volume located at a depth z_t in the sample and of thickness $\delta z_t \sim c_0\lambda^2/(2n_0\Delta\lambda) \sim 3.5$ μm. When the focusing plane and the coherence volume coincide (Fig. 2a$_1$), an holoscopic image of the sample, $\mathbf{I}_H$, can be obtained for each input wave-front $\mathbf{u}_{\rm in}$ (Fig. 2a$_1$):

$$I_H(\mathbf{r}_t, \mathbf{u}_{\rm in}) = R(\boldsymbol{\rho}_{\rm out}, \mathbf{u}_{\rm in}, z_t, t). \tag{7}$$

with $\mathbf{r}_t = (\boldsymbol{\rho}_{\rm out}, z_t)$. In practice, an exact matching between the focusing plane and coherence volume is difficult to obtain especially for deep imaging (*i.e* low single-to-multiple scattering ratio). We will describe further how matrix imaging can provide a robust observable for this fine tuning.

Figures 2a$_2$-a$_4$ display longitudinal and transverse cross-sections of the cornea obtained for a normal incident plane wave (see also Supplementary Movies 1 and 2). Although this holoscopic image can be obtained at a very high frame rate ($Fps \sim 10^{12}$ pixel/s), it also exhibits a speckle-like feature. Indeed, multiply-scattered photons taking place ahead of the coherence volume at each time t can pollute the image. Such paths generate a random speckle noise without any connection with the medium reflectivity. To remove it, a naive strategy is to sum the intensity of the holoscopic images obtained for each illumination $\mathbf{u}_{\rm in}$. Such an incoherent compound tends to smooth out the speckle noise but the resulting image still exhibits an extremely low contrast due to the multiple scattering background (see Supplementary Fig. S2). To get rid of it, the single-to-multiple scattering ratio shall be increased[18]. For this purpose, a spatial filtering of multiply-scattered photons can be performed by means of a confocal filter. Nevertheless, this operation is extremely sensitive to the focusing quality inside the sample. A prior optimization of the focusing process is thus needed.

Digital confocal imaging.

To that aim, the reflection matrix is projected in the focused basis both at input

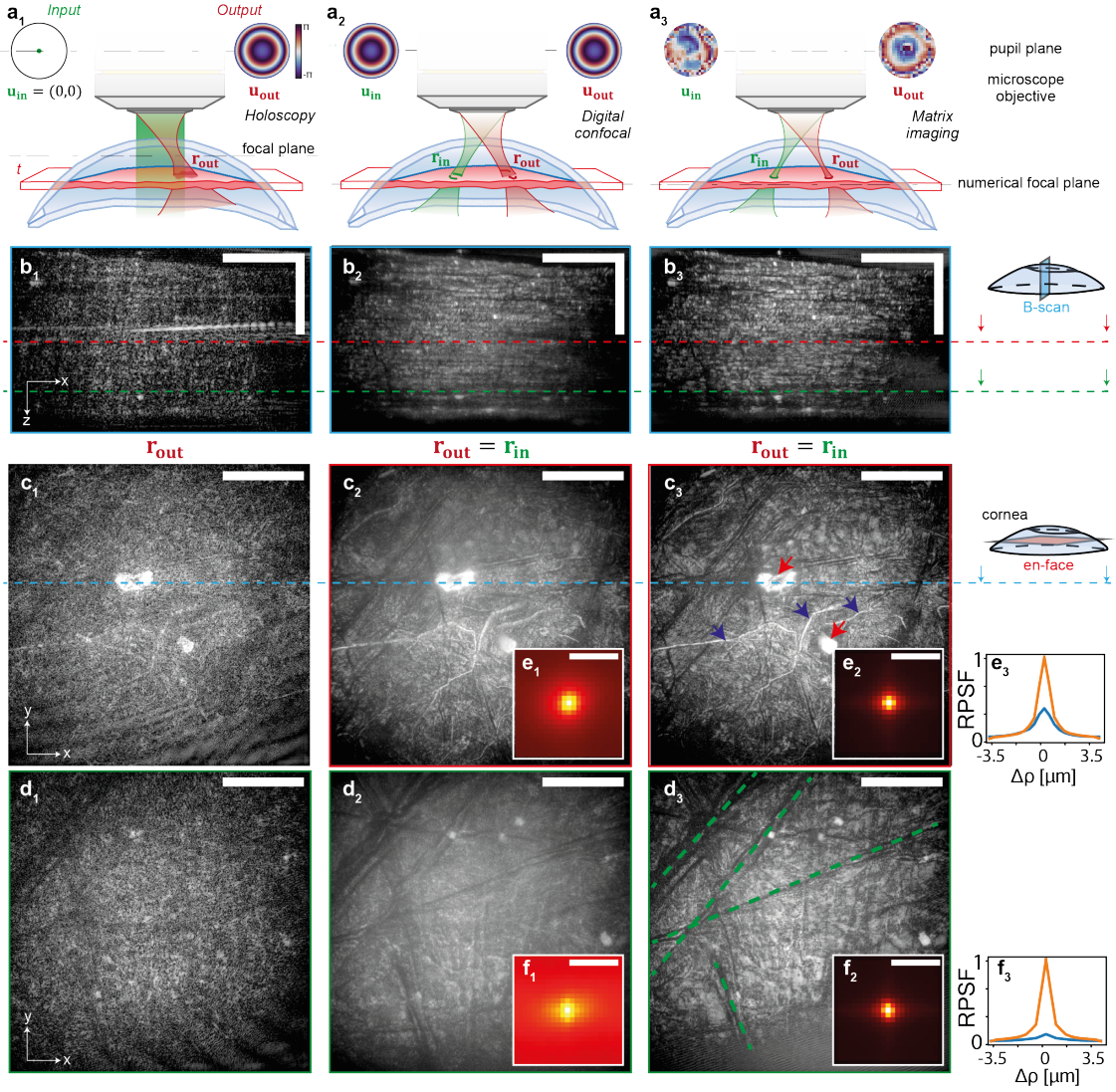

FIG. 2. **From Holoscopy to Matrix Imaging.** **a**, Imaging Methods. $\mathbf{a}_1$, Holoscopy: The sample is illuminated by a plane wave (in green) and an image is produced by spatio-temporal focusing of the back-scattered wave-field on each voxel $\mathbf{r}_{\text{out}}$ mapping the sample (red). $\mathbf{a}_2$, Digital confocal imaging: The sample is illuminated by a set of plane waves (in green) and a focused refection matrix $\mathbf{R}_{\boldsymbol{\rho\rho}}(z_t)$ is built by numerical focusing. A 3D confocal image is deduced from the diagonal elements of $\mathbf{R}_{\boldsymbol{\rho\rho}}(z)$ at each depth z_t. $\mathbf{a}_3$, Reflection matrix imaging: A local compensation of wave distortions is performed for each voxel. **b**, B-scan image showing one longitudinal section of the cornea reflectivity. **c-d**, En-face image of the cornea at $z = 150$ μm and 275 μm, respectively [scale bar: 75 μm]. In panels (**a**)-(**d**), subscripts 1, 2 and 3 stand for holoscopy, digital confocal and RMI, respectively. **e**, RPSF at depth $z = 150$ μm [scale bar: 3 μm] for digital confocal ($\mathbf{e}_1$-$\mathbf{f}_1$) and RMI ($\mathbf{e}_2$-$\mathbf{f}_2$) images. The radial evolutions of these RPSFs are compared in panel ($\mathbf{e}_3$) [DCM: blue; RMI: orange]. **f**, Same as in panel (**e**) but at depth $z = 275$ μm.

and output. Mathematically, it simply consists in a numerical input focusing of $\mathbf{R}_{\boldsymbol{\rho}\mathbf{u}}$ using the Fresnel propagator $\mathbf{F}_{\mathbf{u}}$ (Eq. 4):

$$\mathbf{R}_{\boldsymbol{\rho}\boldsymbol{\rho}}(z,t) = \sum_{\omega} \mathbf{R}_{\boldsymbol{\rho}\mathbf{u}}(z,\omega) \times [\mathbf{T}_{\mathbf{u}\boldsymbol{\rho}}(\omega) \circ \mathbf{F}^{*}_{\mathbf{u}}(z,\omega)] e^{j\omega t}. \tag{8}$$

where the symbol $*$ stands for phase conjugate. Expressed in the focused basis, the reflection matrix $\mathbf{R}_{\boldsymbol{\rho}\boldsymbol{\rho}}(z,t)$ contains the responses at each echo time t between virtual sensors of expected positions $\mathbf{r}_{\text{in}} = (\boldsymbol{\rho}_{\text{in}}, z)$ and $\mathbf{r}_{\text{out}} = (\boldsymbol{\rho}_{\text{out}}, z)$.

At each time-of-flight, the focused $\mathbf{R}$-matrix is equivalent to the time-gated reflection matrix considered in previous studies for optical matrix imaging, except that we here have at our disposal a supplementary degree of freedom: The parameter z that controls the axial position of the focusing plane. A raw confocal image $\mathbf{I}_C$ can be built by considering the diagonal elements of $\mathbf{R}_{\boldsymbol{\rho}\boldsymbol{\rho}}$ ($\boldsymbol{\rho}_{\text{in}} = \boldsymbol{\rho}_{\text{out}}$):

$$I_C(\mathbf{r}_t, z) = R(\boldsymbol{\rho}, \boldsymbol{\rho}, z, t). \tag{9}$$

with $\mathbf{r} = (\boldsymbol{\rho}, z_t)$. Figure 3c shows the en-face image obtained at a given time-of-flight t for different values of z. Qualitatively, we see that the image quality strongly depends on the relative position between the coherence volume and the focusing plane. Here the presence of a highly reflecting structure, a corneal nerve, allows us to determine the parameter z that allows to match the focusing plane with the coherence volume.

Self-portrait of the focusing process.

A more quantitative and robust observable is provided by the off-diagonal coefficients of $\mathbf{R}_{\boldsymbol{\rho}\boldsymbol{\rho}}(z,t)$ that enable to probe the focusing quality at any voxel. More precisely, this can be done by investigating the reflection point spread function

(RPSF) defined as follows:

$$RPSF(\Delta\boldsymbol{\rho}, \boldsymbol{\rho}, z, t) = \left|R(\boldsymbol{\rho} - \Delta\boldsymbol{\rho}/2, \boldsymbol{\rho} + \Delta\boldsymbol{\rho}/2, z, t)\right|^2, \tag{10}$$

This quantity derived from the off-diagonal coefficients of $\mathbf{R}_{\boldsymbol{\rho}\boldsymbol{\rho}}$, quantifies the focusing quality for each point $\mathbf{r}_t = (\boldsymbol{\rho}, z_t)$. For a medium of random reflectivity and under a local isoplanatic assumption, its ensemble average actually scales as[25] (Supplementary Section S5):

$$\langle RPSF(\Delta\boldsymbol{\rho}, \boldsymbol{\rho}, z, t)\rangle \propto |H_{\text{in}}|^2 \overset{\Delta\boldsymbol{\rho}}{\circledast} |H_{\text{out}}|^2(\Delta\boldsymbol{\rho}, \boldsymbol{\rho}, z, t) \tag{11}$$

where the symbol $\langle\cdots\rangle$ stands for ensemble average. $H_{\text{in/out}}(\Delta\boldsymbol{\rho}, \boldsymbol{\rho}, z, t)$ is the spatial distribution of the input/output PSF along the de-scanned coordinate $\Delta\boldsymbol{\rho}$ in the coherence plane at z_t when trying to focus at point $(\boldsymbol{\rho}, z)$.

The RPSF can thus provide a self-portrait of the focusing process inside the cornea. Figure 3a shows the evolution of the laterally-averaged RPSF for a given time t as a function of the parameter z in the Fresnel propagator (Eq. 4). As expected, the focusing plane and coherence volume coincide when the RPSF extension is minimized (Fig. 3b), *i.e* for a defocus distance $\Delta z = z - z_t = 0$ (Fig. 3a$_2$). The estimated defocus is roughly constant over the whole thickness of the cornea. This proves that the effective index of the cornea is actually very close to the refractive index n_0 used in our propagation model (see Supplementary Section S6).

Figures 2b$_1$-b−3 displays longitudinal and transverse cross-sections of the confocal image obtained after tuning the coherence volume and focusing plane at any depth (see also Supplementary Movies 3 and 4). The resolution and contrast are much better than the incoherent compound image (Supplementary Fig. S2). In particular, the axial resolution δz_c of the digital confocal image both benefits from the virtual time gating and confocal filter: $\delta z_c = 1/(1/\delta z_t + 2/\delta z_f) \sim 1.1$ μm.

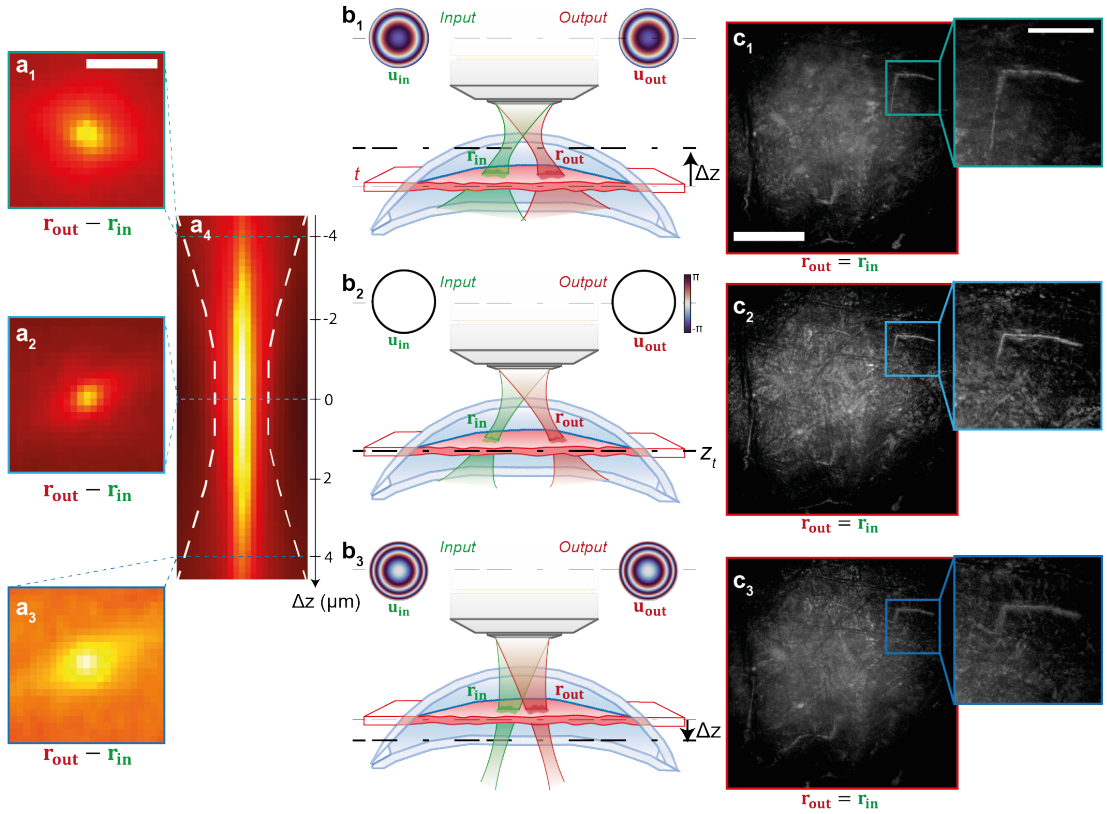

FIG. 3. **Auto-focusing process guided by the reflection point spread function.** **a** Evolution of the RPSF versus the defocus distance Δz for a fixed coherence volume. The transverse distribution of the RPSF is shown for several values of defocus ($\mathbf{a}_1$)-($\mathbf{a}_3$). The evolution of its radial average is displayed in panel ($\mathbf{a}_4$). **b.** Relative position of the focusing plane (dash-dotted line) and coherence volume (red layer) for the different values of defocus Δz displayed in (**a**). **c.** En-face confocal image and zoom on a nerve. In each panel, the subscripts 1, 2 and 3 stand for defocus distances $\Delta z = -4$, 0, and $+4$ μm. The considered coherence volume is located at the effective depth $z_t = 140$ μm in the cornea.

However, the image quality remains perfectible. Indeed, the RPSF still spreads well beyond the theoretical resolution cell ($\sim$ 1 pixel) in Fig. 3a$_2$. These residual aberrations originate from the lateral fluctuations of the optical index $n(\boldsymbol{\rho}, z)$ in the cornea. To demonstrate this last assertion, the transverse evolution of the focusing process can be investigated by a local assessment of the focusing quality (see Methods). A map of local RPSFs is displayed in Fig. 4a. Although the digi-

tal autofocus process provides a correct focusing quality over the whole thickness of the cornea on average, the local RPSFs exhibit important fluctuations across-the field-of-view. This observation is a manifestation of the 3D distribution of the optical index $n(\mathbf{r})$ inside the cornea. This anisoplanic feature requires a local compensation of aberrations as we will see below.

Local Compensation of Wave Distortions.

By considering the set of autofocused reflection matrices, $\mathbf{R}_{\boldsymbol{\rho\rho}}(z_t)$, a local compensation of transverse aberrations can be performed at each depth z_t[16]. It basically consists in a local analysis of wave distortions on overlapping spatial windows of size $L = 18.6$ μm.By exploiting a shift-shift memory effect characteristic of anisotropic scattering in the cornea[26], one can estimate the input and output aberration phase matrices, $\mathbf{\Phi}_{\text{in/out}}(z_t) = [\phi_{\text{in/out}}(\mathbf{u}_{\text{in/out}}, \boldsymbol{\rho}, z_t)]$, between the pupil plane ($\mathbf{u}_{\text{in/out}}$) and the medium voxels ($\boldsymbol{\rho}, z_t$) (Methods)[16]. The result is displayed in Fig. 4b at $z_t = 140$ μm. Strikingly, the estimated aberration laws exhibit strong phase fluctuations and vary quickly between neighboring windows. This complex feature has two origins: (i) the lateral fluctuations exhibited by the optical index inside the cornea; (i) the imperfections of the imaging system. The latter component accounts for the difference observed between the input and output aberration transmittances (Supplementary Section S4). In fact, the input aberration phase law accumulates not only the input aberrations of the sample-arm but also those of the reference arm. The sample-induced aberrations can be investigated independently from the imperfections of the experimental set up by considering the output aberration phase matrix $\boldsymbol{\phi}_{\mathbf{u}}^{(\text{out})}$. The aberration phase is mainly a defocus that varies across the field-of-view due to lateral variations of the optical index. Local shifts of the pupil function are also observed and result from a local curvature of the coherence volume with respect to the focusing plane.

The extracted aberration phase laws can be used to build focusing matrices $\mathbf{G}_{\text{in/out}}$ containing the estimated impulse responses between the image voxels

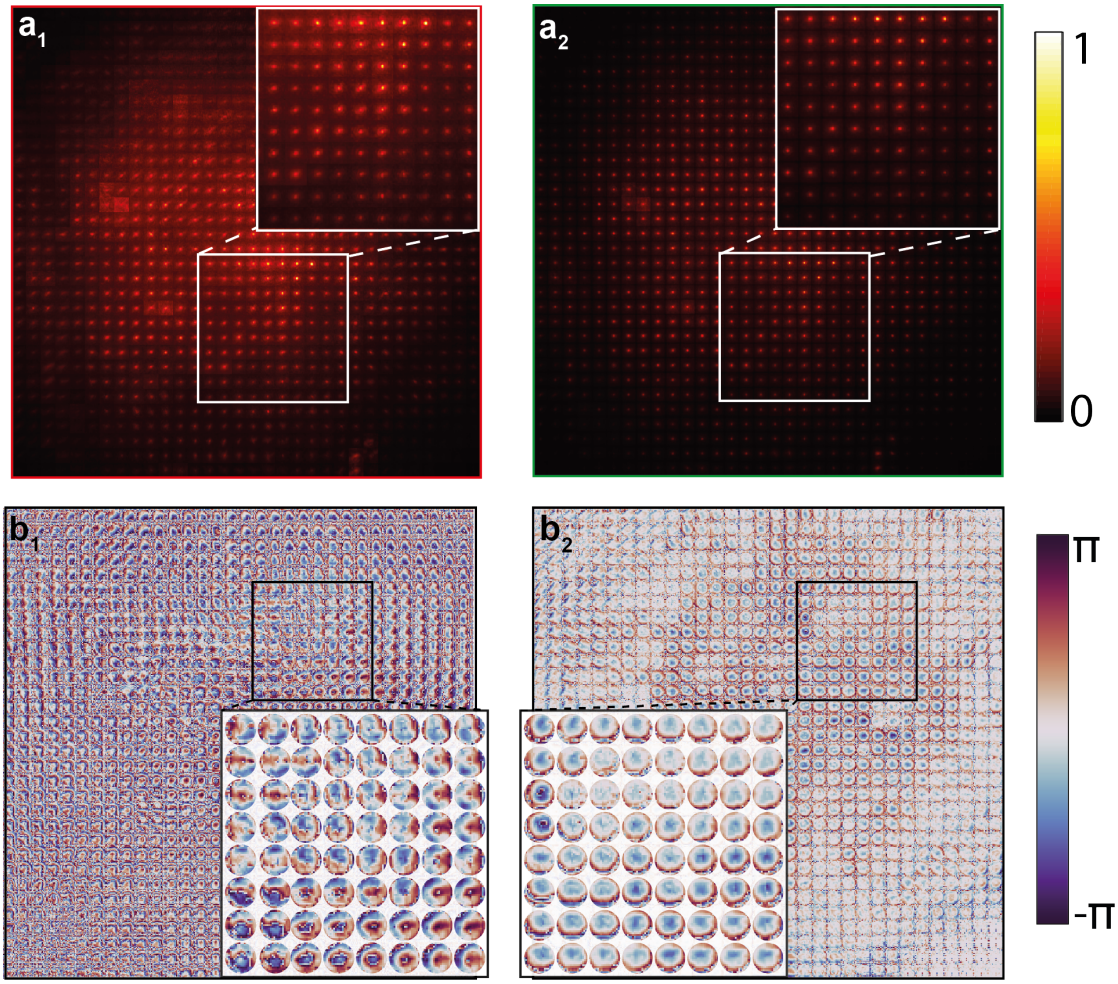

FIG. 4. **Local Adaptive Focusing by Matrix Analysis of Wave Distortions.** **a**, Transverse map of local RPSFs after the auto-focusing process ($\mathbf{a}_1$) and after the aberration matrix compensation of wave distortion ($\mathbf{a}_2$) at $z_t = 140$ μm Each RPSF is displayed over a de-scan area of 6×6 μm^2. **b**, Transverse map of input ($\mathbf{b}_1$) and output ($\mathbf{b}_2$) aberration phase laws, $\phi_{\text{in/out}}$, estimated from the pupil plane at the same depth.

($\boldsymbol{\rho}_{\text{in/out}}$) and the focal plane at each depth z_t:

$$\mathbf{G}_{\text{in/out}}(z_t) = \left\{\mathbf{T}_{\mathbf{u}\boldsymbol{\rho}} \circ \exp\left[i\boldsymbol{\Phi}_{\text{in/out}}(z_t)\right]\right\} \times \mathbf{T}^{\dagger}_{\mathbf{u}\boldsymbol{\rho}} \tag{12}$$

The focused $\mathbf{R}-$matrix is then de-convolved by applying the phase conjugate of

the focusing matrices at its input and output (Fig. 2a$_3$), such that:

$$\mathbf{R}^{(\mathrm{c})}_{\boldsymbol{\rho\rho}}(z_t) = \mathbf{G}^{\dagger}_{\mathrm{out}}(z_t) \times \mathbf{R}_{\boldsymbol{\rho\rho}}(z_t) \times \mathbf{G}^{*}_{\mathrm{in}}(z_t) \tag{13}$$

The final image of the sample can be obtained by considering the diagonal elements of the corrected matrix $\mathbf{R}^{(\mathrm{c})}_{\boldsymbol{\rho\rho}}$:

$$I_M(\mathbf{r}_t) = R^{(\mathrm{c})}(\boldsymbol{\rho}, \boldsymbol{\rho}, z_t). \tag{14}$$

Figures 2c$_3$-e$_3$ display the corresponding longitudinal and transverse cross-sections of the matrix image (see also Supplementary Movies 5, 6 and 7). The comparison with the confocal image [Figs. 2c$_2$-e$_2$] shows a clear gain in contrast. The resolution improvement can be assessed by examining the RPSF. While, at the previous step, the confocal peak exhibits a spreading well beyond the diffraction limit and a background at depth due to forward multiple scattering events (Fig. 2e$_1$,f$_1$), matrix imaging compensates for these two issues and leads to an almost ideal RPSF (Fig. 2e$_2$,f$_2$). The map of final RPSFs displayed by Fig. 4c$_3$ shows the high focusing quality provided by matrix imaging over the whole field-of-view at the considered depth $z_t = 140$ μm.

The obtained three-dimensional image highlights several crucial features of the cornea: its lamellar structure induced by the collagen fibrils (Fig. 2b$_3$); (*ii*) the complex network of nerves that covers the cornea (blue arrows in Fig. 2c$_3$); (*iii*) characteristic structures of the cornea such as keratocytes (red arrows in Fig. 2c$_3$) and; (*iv*) stromal striae (dashed green lines in Fig. 2d$_3$) whose presence is an indicator of keratoconus[27]. Such a high-resolution image can thus be of particular importance for bio-medical diagnosis, given the high frame rate of our device. Of course, matrix imaging is not limited to the cornea but can be also applied to the deep inspection of retina, skin or arteries, tissues whose structures are already monitored by OCT but, until now, limited by a modest penetration depth. In that

perspective, the ability of matrix imaging in overcoming high-order aberrations and multiple scattering constitutes a paradigm shift for deep optical microscopy.

Discussion

In contrast with previous works that considered the reflection matrix at a single frequency[28] or time-of-flight[10,11,14], the measurement of a polychromatic reflection matrix[20] allowed us to realize in post-processing: (i) a 3D confocal image of the sample reflectivity on millimetric volumes (0.1 mm^3 = 10^9 pixels) in an ultra-fast acquisition time (1 s); (ii) a local compensation of aberrations which usually prevent deep imaging. Compared to a time-gated reflection matrix that only allows a transverse compensation of aberrations, the polychromatic reflection matrix gives access to temporal degrees of freedom that can be exploited for compensating the axial distortions of the coherence volume. Eventually, it can be exploited for overcoming the multiple scattering limit in optical microscopy since it provides the opportunity of tailoring complex spatio-temporal focusing laws[19] required to focus light in depth.

To do so, the mapping of the refractive index will also be an important step to build accurate focusing laws inside the medium[29]. As shown by quantitative phase imaging of thin biological samples, this physical parameter is also a quantitative marker for biology. Mapping the refractive index in 3D and in an epi-detection geometry will pave the way towards a quantitative imaging of biological tissues.

In that perspective, an issue we have not considered yet is medium motion during the acquisition of the reflection matrix. Of course, the assumption of a static medium is everything but true especially for in-vivo applications[30]. To cope with the dynamic features of the medium, two strategies can be followed. The first one is to limit the measurement time of the $\mathbf{R}$-matrix at its minimum, as allowed by our device using a few illuminations. The second one is to develop algorithms that consider medium motion during the measurement of $\mathbf{R}$[31]. Interestingly, temporal fluctuations of the medium's reflectivity and refractive index can provide a key

information for probing the multi-cellular dynamics in optical microscopy[32,33]. By its frame rate and volumetric capabilities, our device will constitute an ideal tool for probing the 3D dynamics of tissues in a near future.

Methods

Experimental components.

The following components were used in the experimental setup (Fig. 1): A swept laser source (800-875 nm; Superlum-850 HP), one galvanometer (Thorlabs, LSKGG4), one scan lens L_1 ($f_1 = 110$ mm), two immersion objective lenses (40×; NA, 0.8; Nikon), an imaging lens L_2 ($f_2 = 250$ mm) and an ultrafast camera (25 kHz; Phantom-v2640).

Sample preparation.

In the presented experiment, the corneal sample was fixed with paraformaldehyde (4% concentration).

Sampling of input and output wave-fields.

The dimension of the input pupil is $D_{in} \times D_{in} = 9 \times 9$ mm; the spatial sampling of input wave-fields is $\delta u_{\text{in}} = 600\mu$m. Given the magnification of the output lens system (MO, L_2) system MO1 and the inter-pixel distance of the camera ($\delta s_{\text{out}} = 12\ \mu$m), the output wave-field is sampled at a resolution close to $\lambda/(4NA)$: $\delta\boldsymbol{\rho}_{out} = 290$ nm.

Data acquisition and GPU processing.

All the interferograms of the acquisition sequence are recorded by the camera in 1.4 s and stored in its internal memory. Then, the whole data set (75 Go) is transferred to the computer in 5 min. The numerical post-processing of the reflection matrix is performed by GPU (NVIDIA TITAN RTX) and takes 3.6 s per input wave-fronts. For the data set considered in this paper, all the focusing and aberration correction algorithms are performed in 1 hour.

On-axis holography.

For each input wave-field, the interferogram recorded by the camera can be

expressed as follows:

$$I(\mathbf{s}_{\text{out}}, \mathbf{u}_{\text{in}}, \omega) = |R(\mathbf{s}_{\text{out}}, \mathbf{u}_{\text{in}},\omega) + R_{\text{ref}}(\mathbf{s}_{\text{out}}, \mathbf{u}_{\text{in}}, \omega)|^2 \tag{15}$$

with R and R_{ref}, the wave-fields reflected by the sample and reference arms. Then a Fourier transform in the frequency domain is performed. The resulting intensity can be written as follows:

$$I(\mathbf{s}_{\text{out}}, \mathbf{u}_{\text{in}}, t) = R(\mathbf{s}_{\text{out}}, \mathbf{u}_{\text{in}}, t) \overset{t}{\circledast} R^*(\mathbf{s}_{\text{out}}, \mathbf{u}_{\text{in}}, -t) \tag{16}$$

$$+ R_{\text{ref}}(\mathbf{s}_{\text{out}}, \mathbf{u}_{\text{in}}, -t) \overset{t}{\circledast} R^*_{\text{ref}}(\mathbf{s}_{\text{out}}, \mathbf{u}_{\text{in}}, -t) \tag{17}$$

$$+ R_{\text{ref}}(\mathbf{s}_{\text{out}}, \mathbf{u}_{\text{in}}, t) \overset{t}{\circledast} R^*(\mathbf{s}_{\text{out}}, \mathbf{u}_{\text{in}}, -t) \tag{18}$$

$$+ R(\mathbf{s}_{\text{out}}, \mathbf{u}_{\text{in}}, t) \overset{t}{\circledast} R^*_{\text{ref}}(\mathbf{s}_{\text{out}}, \mathbf{u}_{\text{in}}, -t) \tag{19}$$

where the symbol $\circledast$ stands for the convolution product. The two first terms (Eqs. 16 and 17) correspond to the self-interference of each arm with itself. Both contributions emerge at an optical depth close to zero ($t = 0$). The two last terms correspond to the anti-causal (Eq. 18) and causal (Eq. 19) components of the interference between the two arms. By applying a Heavyside filter to $I(\mathbf{s}_{\text{out}}, \mathbf{u}_{\text{in}}, t)$ along the time dimension, one can isolate the causal contribution (Eq. 19). An inverse Fourier transform then yields the distorted wave-field $D(\mathbf{s}_{\text{out}}, \mathbf{u}_{\text{in}}, \omega) = R(\mathbf{s}_{\text{out}}, \mathbf{u}_{\text{in}}, \omega)R^*_{\text{ref}}(\mathbf{s}_{\text{out}}, \mathbf{u}_{\text{in}}, \omega)$. If aberrations in the reference are neglected (Supplementary Section S3), the reference wave-field is a replica of the incident wave-field,

$$R_{\text{ref}}(\mathbf{s}_{\text{out}}, \mathbf{u}_{\text{in}}, \omega) = \exp\left(i\frac{2\pi}{\lambda f}\mathbf{u}_{\text{in}}.\mathbf{s}_{\text{out}}\right)$$

. The multi-spectral reflection matrix is thus extracted using the following relation:

$$\mathbf{R}_{\mathbf{su}}(\omega) = \mathbf{D}_{\mathbf{su}}(\omega) \circ \mathbf{R}_{\text{ref}}(\omega) \tag{20}$$

where the symbol $\circ$ accounts for the Hadamard (term-by-term) product.

Local estimation of focusing quality

To probe the local RPSF, the field-of-view is divided at each effective depth z_t into regions that are defined by their central midpoint $\boldsymbol{\rho}_\mathrm{p}$ and their spatial extension L. A local average of the back-scattered intensity can then be performed in each region:

$$RPSF_l(\Delta\boldsymbol{\rho}, \boldsymbol{\rho}_p, z, z_t) = \langle |R(\boldsymbol{\rho} + \Delta\boldsymbol{\rho}/2, \boldsymbol{\rho} - \Delta\boldsymbol{\rho}/2, z, t)|^2 W_L(\boldsymbol{\rho} - \boldsymbol{\rho}_p)\rangle_{\boldsymbol{\rho}} \tag{21}$$

where the symbol $\langle \cdots \rangle_x$ stands for an average over the variable x in subscript. $W_L(\boldsymbol{\rho} - \boldsymbol{\rho}_p) = 1$ for $|\boldsymbol{\rho} - \boldsymbol{\rho}_\mathrm{p}| < L$, and zero otherwise. In this paper, a spatial window of size $L = 18.6$ μm has been used to smooth out fluctuations due to the sample inhomogeneous reflectivity[25].

Local compensation of wave-distortions

The starting point is the time-gated reflection matrix $\mathbf{R}_{\boldsymbol{\rho}\boldsymbol{\rho}}(z_t)$, obtained after tuning the focusing plane and coherence volume at each echo time t. The first step is a projection of $\mathbf{R}_{\boldsymbol{\rho}\boldsymbol{\rho}}(z_t)$ in the pupil plane at input via a numerical Fourier transform:

$$\mathbf{R}_{\boldsymbol{\rho}\mathbf{u}}(z_t) = \mathbf{T}^{\top}_{\mathbf{u}\boldsymbol{\rho}}(\omega_c) \times \mathbf{R}_{\boldsymbol{\rho}\boldsymbol{\rho}}(z_t) \tag{22}$$

An input distortion matrix is then built by performing a element-wise product between $\mathbf{R}_{\mathbf{u}\boldsymbol{\rho}}(z_t)$ and the phase conjugate reference matrix $\mathbf{T}_{\mathbf{u}\boldsymbol{\rho}}(\omega_c)$ that would be obtained in absence of aberrations[13] (Supplementary Section S7):

$$\mathbf{D}_{\boldsymbol{\rho}\mathbf{u}}(z_t) = \mathbf{R}_{\boldsymbol{\rho}\mathbf{u}}(z_t) \circ \mathbf{T}^{*}_{\mathbf{u}\boldsymbol{\rho}}(\omega_c) \tag{23}$$

A local correlation matrix $\mathbf{C}_\mathrm{in}$ of wave distortions is then built around each point

$\mathbf{r_p} = (\boldsymbol{\rho}_\mathrm{p}, z_t)$ of the field-of-view (Supplementary Section S8). Its cofficients write:

$$C_\mathrm{in}(\mathbf{u}_\mathrm{in}, \mathbf{u}'_\mathrm{in}, \mathbf{r_p}) = \langle D(\boldsymbol{\rho}_\mathrm{out}, \mathbf{u}_\mathrm{in}, z_t) D(\boldsymbol{\rho}_\mathrm{out}, \mathbf{u}'_\mathrm{in}, z_t) W_L(\boldsymbol{\rho}_\mathrm{out} - \boldsymbol{\rho}_\mathrm{p}) \rangle_{\boldsymbol{\rho}_\mathrm{out}} \tag{24}$$

Iterative phase reversal (see further) is then applied to each correlation matrix $\mathbf{C}_\mathrm{in}(\mathbf{r_p})$[16] (Supplementary Section S9). The resulting input phase laws, $\mathbf{\Phi}_\mathrm{in}(z_t) = [\phi_\mathrm{in}(\mathbf{u}_\mathrm{in}, \boldsymbol{\rho}_p, z_t)]$, are used to compensate for the wave distortions undergone by the incident wave-fronts:

$$\mathbf{R}'_{\boldsymbol{\rho\rho}}(z_t) = \{\mathbf{R}_{\boldsymbol{\rho}\mathbf{u}}(z_t) \circ \exp[-i\boldsymbol{\phi}_\mathrm{in}(z_t)]\} \times \mathbf{T}^*_{\mathbf{u}\boldsymbol{\rho}}(\omega_c) \tag{25}$$

The corrected matrix $\mathbf{R}'_{\boldsymbol{\rho\rho}}$ is only intermediate since phase distortions undergone by the reflected wave-fronts remain to be corrected.

To that aim, $\mathbf{R}'_{\boldsymbol{\rho\rho}}(z_t)$ is now projected in the pupil plane at output:

$$\mathbf{R}'_{\mathbf{u}\boldsymbol{\rho}}(z_t) = \mathbf{T}_{\mathbf{u}\boldsymbol{\rho}}(\omega_c) \times \mathbf{R}'_{\boldsymbol{\rho\rho}}(z_t). \tag{26}$$

An output distortion matrix is then built:

$$\mathbf{D}_{\mathbf{u}\boldsymbol{\rho}}(z_t) = \mathbf{T}^*_{\mathbf{u}\boldsymbol{\rho}}(\omega_c) \circ R'_{\mathbf{u}\boldsymbol{\rho}}(z_t) \tag{27}$$

From $\mathbf{D}_{\mathbf{u}\boldsymbol{\rho}}$, one can build a correlation matrix $\mathbf{C}_\mathrm{out}$ for each point $\mathbf{r_p}$:

$$C_\mathrm{out}(\mathbf{u}_\mathrm{out}, \mathbf{u}'_\mathrm{out}, \mathbf{r_p}) = \langle D(\mathbf{u}_\mathrm{out}, \boldsymbol{\rho}_\mathrm{in}, z_t) D^*_\mathrm{out}(\mathbf{u}'_\mathrm{out}, \boldsymbol{\rho}_\mathrm{in}, z_t) W_L(\boldsymbol{\rho}_\mathrm{in} - \boldsymbol{\rho}_\mathrm{p}) \rangle_{\boldsymbol{\rho}_\mathrm{in}} \tag{28}$$

The IPR algorithm described further is then applied to each matrix $\mathbf{C}_\mathrm{out}(\mathbf{r_p})$. The resulting output phase laws, $\mathbf{\Phi}_\mathrm{out}(z_t) = [\phi_\mathrm{out}(\mathbf{u}_\mathrm{out}, \boldsymbol{\rho_p}, z_t)]$, are leveraged to compensate for the residual wave distortions undergone by the reflected wave-fronts:

$$\mathbf{R}^{(c)}_{\boldsymbol{\rho\rho}}(z_t) = \mathbf{T}^\dagger_{\mathbf{u}\boldsymbol{\rho}}(\omega_c) \times \left\{\exp[-i\boldsymbol{\phi}_\mathrm{out}(z_t)] \circ \mathbf{R}'_{\mathbf{u}\boldsymbol{\rho}}(z_t)\right\} \tag{29}$$

Iterative phase reversal algorithm.

The IPR algorithm is a computational process that provides an estimator of the phase of the transmittance that links each point $\mathbf{u}$ of the pupil plane with each voxel $\mathbf{r_p} = (\boldsymbol{\rho}_p, z_t)$ of the cornea volume[16]. To that aim, the correlation matrix $\mathbf{C}$ computed over the spatial window W_L centered around a given point $(\boldsymbol{\rho}_p, z_t)$ is considered (Eqs. 24 and 28). Mathematically, the algorithm is based on the following recursive relation:

$$\boldsymbol{\Phi}_{\mathbf{u}}^{(n)}(\boldsymbol{\rho}_p, z_t) = \arg\left\{\mathbf{C}(\boldsymbol{\rho}_p, z_t) \times \exp\left[i\boldsymbol{\Phi}_{\mathbf{u}}^{(n-1)}(\boldsymbol{\rho}_p, z_t)\right]\right\} \tag{30}$$

where $\boldsymbol{\Phi}_{\mathbf{u}}^{(n)}$ is the estimator of the transmittance phase at the nth iteration of the phase reversal process. $\boldsymbol{\Phi}_{\mathbf{u}}^{(0)}$ is an arbitrary wave-front that initiates the process (typically a flat phase law) and $\boldsymbol{\phi} = \lim_{n\to\infty} \boldsymbol{\phi}^{(n)}$ is the result of IPR.

Data availability. Optical data used in this manuscript have been deposited at Zenodo

Code availability. Codes used to post-process the optical data within this paper are available from the corresponding author.

Acknowledgments. The authors wish to thank A. Badon for initial discussions on the project, K. Irsch for providing the corneal sample, A. Le Ber for providing the iterative phase reversal algorithm and F. Bureau for his help on Supplementary movies.

Funding Information. The authors are grateful for the funding provided by the European Research Council (ERC) under the European Union's Horizon 2020 research and innovation program (grant agreement nos. 610110 and 819261,

HELMHOLTZ* and REMINISCENCE projects, respectively). This project has also received funding from Labex WIFI (Laboratory of Excellence within the French Program Investments for the Future; ANR-10-LABX-24 and ANR-10-IDEX-0001-02 PSL*) and from CNRS Innovation (Prematuration program, MATRISCOPE project).

Author Contributions. A.A. initiated and supervised the project. P.B., V.B. and A.A. designed the experimental setup. P.B., V.B. and N.R. built the experimental set up. V.B. designed the acquisition scheme. V.B., P.B., N.G. and E.A. developed the post-processing tools. P.B. performed the corneal imaging experiment. V.B., P.B. and A.A. analyzed the experimental results. V.B., P.B. and A.A. performed the theoretical study. P.B., V.B. and A.A. prepared the manuscript. P.B., V.B., N.G., A.C.B., M.F. and A.A. discussed the results and contributed to finalizing the manuscript.

Competing interests. P.B., V.B., M.F., C.B. and A.A. are named inventors on french patent FR2207334 (filing date 18.07.2022), which is related to the techniques described in this Article.

[1] V. Ntziachristos, Going deeper than microscopy: The optical imaging frontier in biology, Nat. Methods **7**, 603 (2010).

[2] S. Gigan, Optical microscopy aims deep, Nature Photon. **11**, 14 (2017).

[3] M. J. Booth, Adaptive optical microscopy: the ongoing quest for a perfect image, Light Sci. Appl. **3**, e165 (2014).

[4] T.-W. Wu and M. Cui, Numerical study of multi-conjugate large area wavefront correction for deep tissue microscopy, Opt. Express **23**, 7463 (2015).

[5] J.-H. Park, Z. Yu, K. Lee, P. Lai, and Y. Park, Perspective: Wavefront shaping techniques for controlling multiple light scattering in biological tissues, APL Photonics **3**, 100901 (2018).

[6] T. S. Ralston, D. L. Marks, P. S. Carney, and S. A. Boppart, Interferometric synthetic aperture microscopy, Nat. Phys. **3**, 129 (2007).

[7] S. G. Adie, B. W. Graf, A. Ahmad, P. S. Carney, and S. A. Boppart, Computational adaptive optics for broadband optical interferometric tomography of biological tissue, Proc. Nat. Acad. Sci. USA **109**, 7175 (2012).

[8] A. Ahmad, N. D. Shemonski, S. G. Adie, H.-S. Kim, W.-M. W. Hwu, P. S. Carney, and S. A. Boppart, Real-time in vivo computed optical interferometric tomography, Nat. Photon. **7**, 444 (2013).

[9] D. Hillmann, H. Spahr, C. Hain, H. Sudkamp, G. Franke, C. Pfäffle, C. Winter, and G. Hüttmann, Aberration-free volumetric high-speed imaging of in vivo retina, Sci. Rep. **6**, 35209 (2016).

[10] S. Kang, S. Jeong, W. Choi, H. Ko, T. D. Yang, J. H. Joo, J.-S. Lee, Y.-S. Lim, Q.-H. Park, and W. Choi, Imaging deep within a scattering medium using collective accumulation of single-scattered waves, Nat. Photonics **9**, 253 (2015).

[11] A. Badon, D. Li, G. Lerosey, A. C. Boccara, M. Fink, and A. Aubry, Smart optical

coherence tomography for ultra-deep imaging through highly scattering media, Sci. Adv. **2**, e1600370 (2016).

[12] S. Kang, P. Kang, S. Jeong, Y. Kwon, T. D. Yang, J. H. Hong, M. Kim, K.-D. Song, J. H. Park, J. H. Lee, M. J. Kim, K. H. Kim, and W. Choi, High-resolution adaptive optical imaging within thick scattering media using closed-loop accumulation of single scattering, Nat. Commun. **8**, 2157 (2017).

[13] A. Badon, V. Barolle, K. Irsch, A. C. Boccara, M. Fink, and A. Aubry, Distortion matrix concept for deep optical imaging in scattering media, Sci. Adv. **6**, eaay7170 (2020).

[14] S. Yoon, H. Lee, J. H. Hong, Y.-S. Lim, and W. Choi, Laser scanning reflection-matrix microscopy for aberration-free imaging through intact mouse skull, Nat. Commun. **11**, 5721 (2020).

[15] Y. Kwon, J. H. Hong, S. Kang, H. Lee, Y. Jo, K. H. Kim, S. Yoon, and W. Choi, Computational conjugate adaptive optics microscopy for longitudinal through-skull imaging of cortical myelin, Nat. Commun. **14**, 105 (2023).

[16] U. Najar, V. Barolle, P. Balondrade, M. Fink, A. C. Boccara, M. Fink, and A. Aubry, Non-invasive retrieval of the transmission matrix for optical imaging deep inside a multiple scattering medium, arXiv: 2303.06119 (2023).

[17] D. Huang, E. Swanson, C. Lin, J. Schuman, W. Stinson, W. Chang, M. Hee, T. Flotte, K. Gregory, C. Puliafito, *et al.*, Optical coherence tomography, Science **254**, 1178 (1991).

[18] A. Badon, A. C. Boccara, G. Lerosey, M. Fink, and A. Aubry, Multiple scattering limit in optical microscopy, Opt. Express **25**, 28914 (2017).

[19] Y.-R. Lee, D.-Y. Kim, Y. Jo, M. Kim, and W. Choi, Exploiting volumetric wave correlation for enhanced depth imaging in scattering medium, Nat. Commun. **14** (2023).

[20] Y. Zhang, D. Minh, Z. Wang, T. Zhang, T. Chen, and C. W. Hsu, Deep

imaging inside scattering media through virtual spatiotemporal wavefrontshaping, arXiv:2306.08793 (2023).

[21] B. Považay, A. Unterhuber, B. Hermann, H. Sattmann, H. Arthaber, and W. Drexler, Full-field time-encoded frequency-domain optical coherence tomography, Opt. Express **14**, 7661 (2006).

[22] D. Hillmann, G. Franke, C. Lührs, P. Koch, and G. Hüttmann, Efficient holoscopy image reconstruction, Opt. Express **20**, 21247 (2012).

[23] E. Auksorius, D. Borycki, P. Stremplewski, K. Lizewski, S. Tomczewski, P. Niedzwiedziuk, B. L. Sikorski, and M. Wojtkowski, In vivo imaging of the human cornea with high-speed and high-resolution fourier-domain full-field optical coherence tomography, Biomed. Opt. Exp. **11**, 2849 (2020).

[24] P. Stremplewski, E. Auksorius, P. Wnuk, L. Kozon, P. Garstecki, and M. Wojtkowski, In vivo volumetric imaging by crosstalk-free full-field OCT, Optica **6**, 608 (2019).

[25] W. Lambert, L. A. Cobus, M. Couade, M. Fink, and A. Aubry, Reflection Matrix Approach for Quantitative Imaging of Scattering Media, Phys. Rev. X **10**, 021048 (2020).

[26] B. Judkewitz, R. Horstmeyer, I. M. Vellekoop, I. N. Papadopoulos, and C. Yang, Translation correlations in anisotropically scattering media, Nat. Phys. **11**, 684 (2015).

[27] K. Grieve, D. Ghoubay, C. Georgeon, G. Latour, A. Nahas, K. Plamann, C. Crotti, R. Bocheux, M. Borderie, T.-M. Nguyen, F. Andreiuolo, M.-C. Schanne-Klein, and V. Borderie, Stromal striae: a new insight into corneal physiology and mechanics, Sci. Rep. **7**, 13584 (2017).

[28] S. M. Popoff, A. Aubry, G. Lerosey, M. Fink, A. C. Boccara, and S. Gigan, Exploiting the Time-Reversal Operator for Adaptive Optics, Selective Focusing, and Scattering Pattern Analysis, Phys. Rev. Lett. **107**, 263901 (2011).

[29] M. Chen, D. Ren, H.-Y. Liu, S. Chowdhury, and L. Waller, Multi-layer born multiple-scattering model for 3d phase microscopy, Optica **7**, 394 (2020).

[30] M. Jang, H. Ruan, I. M. Vellekoop, B. Judkewitz, E. Chung, and C. Yang, Relation between speckle decorrelation and optical phase conjugation (OPC)-based turbidity suppression through dynamic scattering media: a study on in vivo mouse skin, Biomed. Opt. Express **6**, 72 (2014).

[31] M. Kang, W. Choi, W. Choi, and Y. Choi, Fourier holographic endoscopy for imaging continuously moving objects, Opt. Express **31**, 11705 (2023).

[32] C. Apelian, F. Harms, O. Thouvenin, and A. C. Boccara, Dynamic full field optical coherence tomography: subcellular metabolic contrast revealed in tissues by interferometric signals temporal analysis, Biomed. Opt. Express **7**, 1511 (2016).

[33] J. Scholler, K. Groux, O. Goureau, J.-A. Sahel, M. Fink, S. Reichman, C. Boccara, and K. Grieve, Dynamic full-field optical coherence tomography: 3d live-imaging of retinal organoids, Light Sci. Appl. **9**, 140 (2020).